JOURNAL OF GEOPHYSICAL RESEARCH, VOL. 111, A10S19, doi:10.1029/2006JA011795, 2006

Effect of atmospheric tides on the morphology of the quiet time, postsunset equatorial ionospheric anomaly

S. L. England,[1] T. J. Immel,[1] E. Sagawa,[2] S. B. Henderson,[3] M. E. Hagan,[4] S. B. Mende,[1] H. U. Frey,[1] C. M. Swenson,[3] and L. J. Paxton[5]

Received 18 April 2006; revised 7 August 2006; accepted 13 September 2006; published 31 October 2006.

[1] Recent global-scale observations of the postsunset equatorial O^+ airglow bands in the *F* region ionosphere using the IMAGE FUV and TIMED GUVI have revealed a longitudinal wave number four pattern in the magnetic latitude and concentration of the *F* region peak ion density when measured at a fixed local time. In a new comparison of two data sets with observations made by the OGO 4 satellite, this pattern is seen to be persistent over many days around equinox during magnetically quiet conditions close to solar maximum but can be dominated by other processes such as cross-equator winds during other periods. It is found that the longitudinal variability is created by a processes occurring in the dayside ionosphere. A longitudinal modulation of the dayside equatorial fountain is the most likely driving mechanism. Through comparison with GWSM-02 model, it is shown that the predicted modulation of the dayside thermospheric winds and temperatures at *E* region altitudes created by non-migrating diurnal tides can explain the modulation in the dayside equatorial fountain. This result highlights the importance of understanding the temporal variability of tropospheric weather systems on our understanding and possible predictability of the development of the *F* region ionosphere. It may also provide a possible further means of testing our understanding of atmospheric tides on a global scale.

Citation: England, S. L., T. J. Immel, E. Sagawa, S. B. Henderson, M. E. Hagan, S. B. Mende, H. U. Frey, C. M. Swenson, and L. J. Paxton (2006), Effect of atmospheric tides on the morphology of the quiet time, postsunset equatorial ionospheric anomaly, *J. Geophys. Res.*, *111*, A10S19, doi:10.1029/2006JA011795.

1. Introduction

[2] The highest ion densities in the *F* region of the ionosphere are found to be located several degrees to either side of the magnetic equator [*Namba and Maeda*, 1939; *Appleton*, 1946]. Known as the equatorial ionospheric anomaly (EIA hereafter), this feature is created in a process known as the ''fountain effect,'' which consists of the uplift of plasma at the magnetic equator by eastward electric fields [*Martyn*, 1947, 1953] and subsequent redistribution of along the magnetic field lines to higher latitudes [*Hanson and Moffett*, 1966]. During magnetically quiet periods, the principal source of these electric fields during the daytime is tidal wind motions in the dayside E-region, which drive daytime Pedersen currents [*Kato*, 1956, 1957] that produce a build up of electrical charge along the terminator. Furthermore, polarization charges associated with the action of the *F* region dynamo [*Rishbeth*, 1971] map into the *E* region and are responsible for the sharp enhancement in the vertical drifts around sunset (known as the prereversal enhancement) [*Woodman*, 1970; *Farley et al.*, 1986], far exceeding the effect of the rapidly weakening dayside equatorial fountain during this local time (LT hereafter) period (it is worth noting that these two systems are coupled). While the *E* region dynamo and the daytime vertical drift it drives exhibit only minor variations with solar activity, the *F* region dynamo and prereversal enhancement vary strongly with solar 10.7 cm radio flux (F10.7) [*Fejer et al.*, 1991] as the strength of the associated polarization electric fields vary as ratio of the height-integrated Pedersen conductivities in the *E* and *F* regions. This system can be perturbed by electric fields of magnetospheric origin, but this report will only focus upon the quiet-time state of this system.

[3] Early observations of longitudinal variations in the EIA have been reviewed by *Walker* [1981]. At *F* region heights, cross-equator winds (in magnetic coordinates) flowing from the subsolar point force plasma across the magnetic equator [e.g., *Hanson and Moffett*, 1966; *Bramley and Young*, 1968; *Thuillier et al.*, 2002] producing an asymmetry in the EIA about the magnetic equator [*Lyon and Thomas*, 1963; *Thomas*, 1968; *Bramley and Young*,

[1]Space Sciences Laboratory, University of California, Berkeley, California, USA.
[2]National Institute of Information and Communications Technology, Tokyo, Japan.
[3]Department of Electrical and Computer Engineering, Utah State University, Logan, Utah, USA.
[4]High Altitude Observatory, National Center for Atmopsheric Research, Boulder, Colorado, USA.
[5]Johns Hopkins University Applied Physics Laboratory, Laurel, Maryland, USA.

0148-0227/06/2006JA011795$09.00

1968]. The effect of these winds varies as a function of longitude because of the offset between the magnetic and geographic equators and the change in magnetic declination with longitude [*Challinor and Eccles*, 1971; *Eccles et al.*, 1971; *Thuillier and Blamont*, 1973]. As these cross-equatorial winds are strongest around solstice, these effects can be more easily identified in observations and modeled around solstice than around equinox [*Thuillier et al.*, 2002]. The offset between the magnetic and geographic equators also produces a longitudinally varying asymmetry in ionization rates around equinox due to changes in the solar zenith angle along the magnetic equator. In addition, the horizontal magnetic field at the magnetic equator varies as a function of longitude, with a maximum near 100°E which is 1.5 times stronger than the minimum located near 300°E. Each of these effects is able to produce global-scale variations in the EIA, but not the smaller scale variations that are discussed below. It has also been suggested that smaller-scale variations in electric fields may be responsible for smaller-scale variations in the EIA [e.g., *Walker et al.*, 1980], although no definitive picture of their effects on a global scale during magnetically quiet periods has been established.

[4] When considering the structure of the EIA on a global scale, ground-based observations are of limited use due to the limited longitudinal coverage of land masses around the magnetic equator. Space-based observations of the EIA have offered the ability to study the morphology of the EIA on a global scale, provided that LT and geographical dependences can be separated. Using OGO 4 and 6 data, *Thuillier and Blamont* [1973] studied the morphology of the O (^{1}D) 630.0 nm nighttime equatorial airglow arcs during magnetically quiet periods. The authors were able to produce maps of zenithal emission rates and peak emission altitudes at a fixed LT. Using these maps, they showed that the observed asymmetry in the nighttime airglow arcs associated with the EIA could be explained in terms of cross-equatorial winds (in magnetic coordinates). The authors calculated the necessary *F* region meridional winds to be of order 70 ms^{-1}. Later, using simultaneous 630.0 nm emission rates and Doppler wind velocities observed by UARS WINDII observations, *Thuillier et al.* [2002] showed that there was good agreement between the meridional winds and the large-scale asymmetry in 630.0 nm emission rates. This was also well reproduced in NCAR thermosphere-ionosphere electrodynamics general circulation model (TIE-GCM) simulations for solstice conditions, but less well for equinox. Using late afternoon TEC measurements made over the oceans by the dual frequency altimeter on board TOPEX/Poseidon, *Vladimer et al.* [1999] have shown that the TEC in the EIA region displays longitudinal variability which extends over 4 hours of LT and is repeated day-to-day during magnetically quiet conditions ($K_p \leq 4$). While the pattern was observed to vary with season, a clear longitudinal dependence was observed during equinox, summer, and winter. During equinox, the global variation in peak TEC appears to match changes in the magnetic field strength at the equator. Using the global theoretical ionospheric model (GTIM), the authors showed that this global variation during equinox could be reproduced by modifying the GTIM $\mathbf{E} \times \mathbf{B}$ drifts using a weighting factor which varied as a function of longitude. Recently, *Sagawa et al.* [2005], using IMAGE FUV [*Mende et al.*, 2000a, 2000b], have used high-resolution images of the nighttime *F* region O^+ recombination emissions at 135.6 nm to study the longitudinal dependence of the northern airglow arc associated with the postsunset EIA. Unlike the 630.0 nm emissions observed by OGO 4, OGO 6, and UARS, 135.6 nm is not strongly dependent on the emission altitude, but primarily on the product of the ionospheric O^+ and e^- densities. Using observations from March to early June 2002, when the IMAGE spacecraft had a clear view of the northern airglow arc from both favorable orbital geometry and near solar max conditions, the authors found evidence of three defined peaks, separated by approximately 90°, in both nighttime plasma densities and magnetic latitude of the peak. While their analysis did not highlight sufficient data over the American sector, they hypothesized the existence of a fourth peak in this location. The authors showed that this structure was maintained over several hours of LT and drifts east with time, implying that this is created solely by the dayside fountain and prereversal enhancement around sunset and is not produced by any anomalous post-sunset ion production or transport mechanisms. This signature was seen throughout the equinox-to-early-summer data set. *Sagawa et al.* [2005] found that this wave number-4 longitudinal signature could not be explained by magnetic declination, *F* region wind, magnetic field strength or the offset between magnetic and geographic equators and cited lower atmosphere-ionosphere coupling via nonmigrating tides as a possible explanation. Measurements from equinox 2002 (March, April, September, and October) reported by *Henderson et al.* [2005a], using the same emission line observed by TIMED GUVI [*Humm et al.*, 1998; *Paxton et al.*, 1999; *Christensen et al.*, 2003] show a clear wave number-4 signature in the brightness and offset from the magnetic equator of the northern airglow arc, which was also mirrored in the in the offset of the southern arc, although the longitudinal dependence of the brightness of the southern arc did not show this signature. Good symmetry between the northern and southern arcs during these time periods supports the theory that the equatorial fountain was the major factor controlling equatorial *F* region plasma densities during the spring equinox 2002 as suggest by *Sagawa et al.* [2005]. This signature was not seen in the GUVI data at any other time during 2002 to 2003, although emissions were generally much lower in brightness and asymmetry in the anomaly crests was generally much greater, indicating that cross-equator winds were dominating plasma transport and EIA morphology.

[5] In this paper we shall perform a detailed comparison between the FUV and GUVI observations of the nighttime EIA during the March to April 2002 period and explore the possible influence of lower atmosphere tides on the formation of the EIA. As an extension of the hypothesis of *Sagawa et al.* [2005], we shall demonstrate a clear correspondence between the effects of nonmigrating diurnal tides on the lower thermospheric structure and the morphology of the postsunset EIA. The winds at *E* region altitudes, which are known to drive the dayside fountain process, have a significant longitudinal variation associated with nonmigrating diurnal tides. Here we hypothesize that this modulation of the wind alters the strength of the dayside fountain and that this is observed by FUV and GUVI through a change in the postsunset EIA. An initial comparison between the UV

observations and tidal model results has been described in a recent letter [*Immel et al.*, 2006]. Here we shall extend this analysis to include GUVI data from October 2002 as well as OGO D 12 data from October 1967 in order to form a more complete argument for the mechanism that produces these observed effects. In section 2 we shall outline in detail a new analysis of the FUV data and regrouping of the GUVI data to separate vernal and autumnal equinoxes which allows a direct comparison between the observations reported by *Sagawa et al.* [2005] and *Henderson et al.* [2005a] to be made. In section 3 we shall use the data from FUV, GUVI, and OGO D 12 to provide a detailed description of the observed longitudinal dependence of the equatorial airglow bands and associated *F* region O^+ ion densities during magnetically quiet equinoctial periods. In section 4 we shall explain the observed structure in the airglow in terms of changes in daytime *E* region winds and temperatures as predicted by the GSWM-02 tidal model [*Hagan and Forbes*, 2002].

2. Observational Data and Analysis

[6] While observations of the EIA region were made by both FUV and GUVI during 2002 to 2004, as the brightness of nighttime 135.6 nm emissions scale as the square of the *F* region O^+ density, only 2002 offers periods during which the EIA is clearly visible to both instruments and which are sustained over enough time to observe its longitudinal structure. Further, owing to the precession of the IMAGE and TIMED spacecraft orbits, joint observations during in the postsunset LT range are only available around the vernal equinox. *Henderson et al.* [2005a] have shown this time period to be ideal for studying the equatorial fountain effect due to the high degree of symmetry between the northern and southern EIA arcs and the near solar-max conditions.

[7] While both FUV and GUVI made observations of the same emission line in the EIA airglow arcs, a direct comparison between the data presented by *Sagawa et al.* [2005] and *Henderson et al.* [2005a] is not ideal as *Sagawa et al.* [2005] included all data from March to June 2002 whereas *Henderson et al.* [2005a] used data from magnetically quiet periods during March, April, September, and October 2002. In this section, we shall present the data from both instruments using similar analyses to allow a more fair comparison. The data from OGO D 12 that we shall consider here has been previously presented by *Thuillier and Blamont* [1973] and *Thuillier et al.* [2002] so only a brief summary of the key points is necessary here.

[8] The GUVI data is analyzed using a singular value decomposition routine that has been detailed by *Henderson et al.* [2005b]. In brief, this routine estimates the along-track intensity profiles of the EIA. While removing intensity depletions associated with plasma bubbles, this routine extracts the crest maximum intensities and its latitude from these intensity profiles. Intensities from close-to-nadir views are used, so no knowledge of the emission altitude is required for mapping to magnetic coordinates as there is no limb brightening due to viewing at a shallow angle. The data from 2130 to 2230 LT are selected as these occur after the prereversal enhancement has occurred and yet are still sufficiently close to sunset that a clear and bright EIA is visible in the data. In addition, a relatively narrow LT window is required to avoid blurring of any features by nighttime eastward drifts. Because of the precession in LT of the TIMED orbit, only data from 2 to 7 April provides information in this LT window around the vernal equinox of 2002. The data is also sorted for magnetically quiet periods, where the mean K_p over the previous 0–6, 7–12, 12–18, and 18–30 hours must be less than or equal to three. Figure 1 shows the peak emission rates and offset of this peak from the magnetic equator as a function of longitude during this time as observed by GUVI. A second data set exists for 2 to 7 October 2002, which is qualitatively identical to that shown in Figure 1 and as such does not need to be presented here but will be mentioned as part of the discussion in sections 3 and 4.

[9] The TIMED orbit allows imaging of the entire EIA region (all longitudes) in this LT window to be achieved in 1 day. The IMAGE orbit is such that 3 days are required for a complete sample of the EIA within this LT window to be made. This, combined with the natural variability of the EIA brightness means that a larger day window is required to adequately sample EIA emission rates at all longitudes using IMAGE FUV. While data is available over March to June 2002, we shall restrict our analysis of the FUV data to the period 20 March to 20 April, which allows sufficient coverage at all longitudes as well as closely matching the day window used for the GUVI observations. Sorting data for magnetically quiet periods only (as with the GUVI analysis) further restricts the data sampling, but this day window still proves adequate to provide a minimum of fifteen clear observations of the EIA in each ten degree longitude bin.

[10] As the FUV observations are off nadir, knowledge of the emission layer is required to map the observations into geomagnetic coordinates. Figure 2 shows the simulated emission profile from the SAMI2 model [*Huba et al.*, 2000] for the same solar and seasonal conditions as the FUV observations. As can be seen, the peak emission altitude should be close to 350 km altitude, but there is considerable spread in the emission altitude. For our analysis here, we assume a mean emission altitude of 350 km, but for the purposes of our error analysis we shall consider emissions in the range of 300 to 400 km altitude. Using this estimate of the emission altitude, the observations are mapped onto geomagnetic coordinates and the spacecraft to zenith angle is calculated. This is used convert the line of sight emission rates into column emission rates by multiplying the observed emissions by the cosine of this angle. This approximate correction becomes invalid for increasingly large angles, such as for observations of the southern equatorial arc from the IMAGE orbit, and hence we shall only include observations of the northern arc in our analysis.

[11] In order to find the location and peak brightness of the northern EIA arc, the data are first sorted into 15 min LT and 1 degree in longitude bins. Then, to remove noise we fit a Gaussian to these EIA cross sections between the magnetic equator and 30° magnetic latitude. Figure 3 shows the 10 degree longitudinal running mean of the peak emission rates and magnetic latitude of that peak. Errors are estimated from both the spread of values in each 10 degree bin and the uncertainty associated with the emission altitude as described earlier.

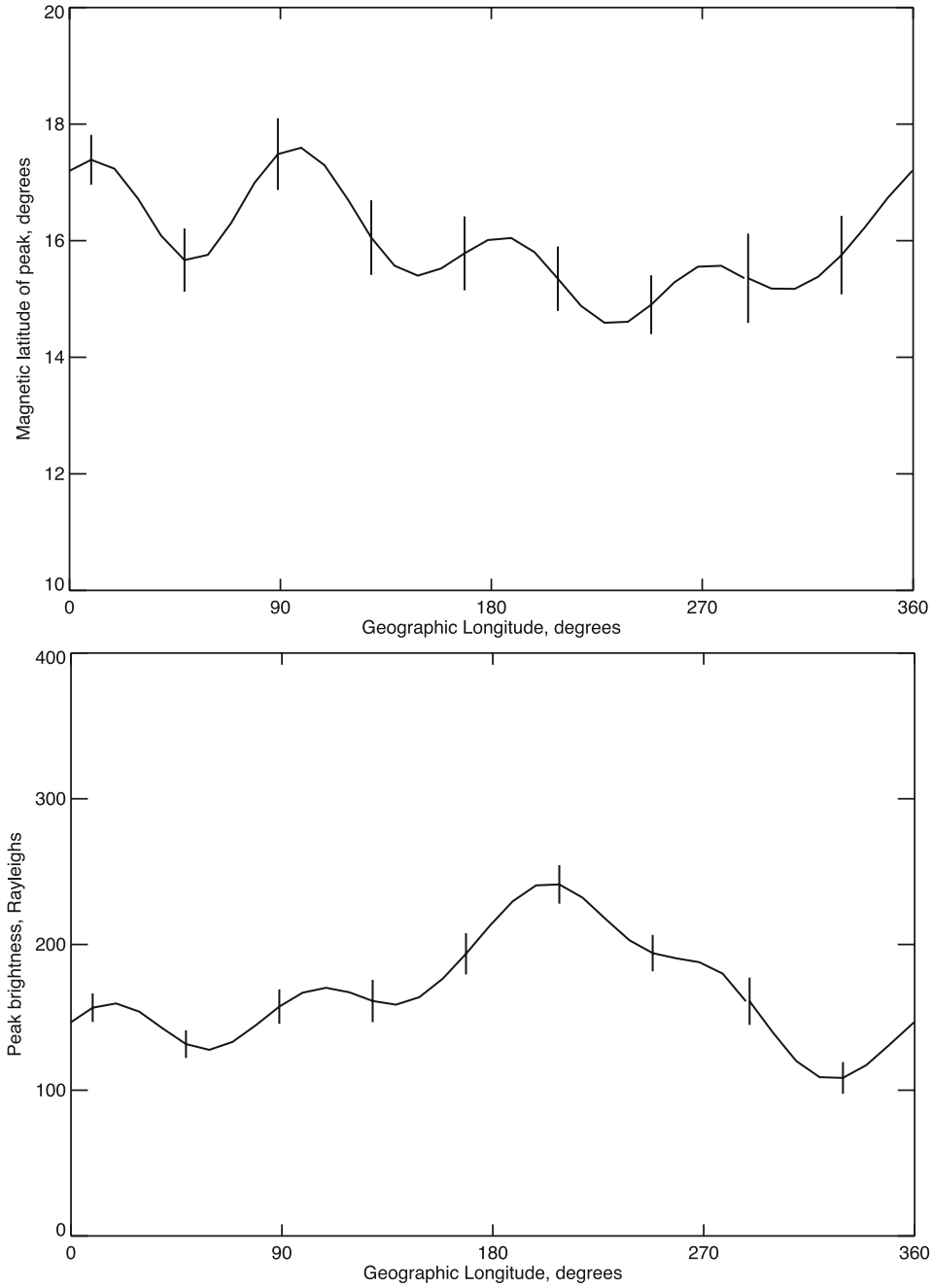

Figure 1. (top) Magnetic latitude of the peak 135.6 nm emission rates and (bottom) brightness of this peak observed in the northern arc of the EIA by TIMED GUVI. Values have been corrected to remove the effects of plasma bubbles and averaged over ten degrees of longitude. Standard errors are shown every 40 degrees of longitude. Only data from 2030 to 2130 LT, between 2 and 7 April 2002 during magnetically quiet periods is shown here.

[12] As the analysis of the FUV data presented here differs greatly from that of *Sagawa et al.* [2005], it is worth briefly addressing the differences between these results. Comparing our Figure 3 to Figures 5 and 6 from *Sagawa et al.* [2005], it is apparent that the relative uncertainties in both position and brightness of the EIA peak have been reduced in our analysis, especially in the Atlantic region. This is because of a combination of restricting our date range to near equinox, using only data from an earlier LT when the EIA brightness was greater (which is especially important in the Atlantic region where the emissions are generally lower), selection for magnetically quiet periods which removes the effects of penetration fields, and removing noise using Gaussian fits to the data and a 10 degree longitudinal running mean. In addition to reducing the uncertainties in the results, our analysis has also highlighted the fourth peak in brightness and magnetic latitude of the EIA in the American sector

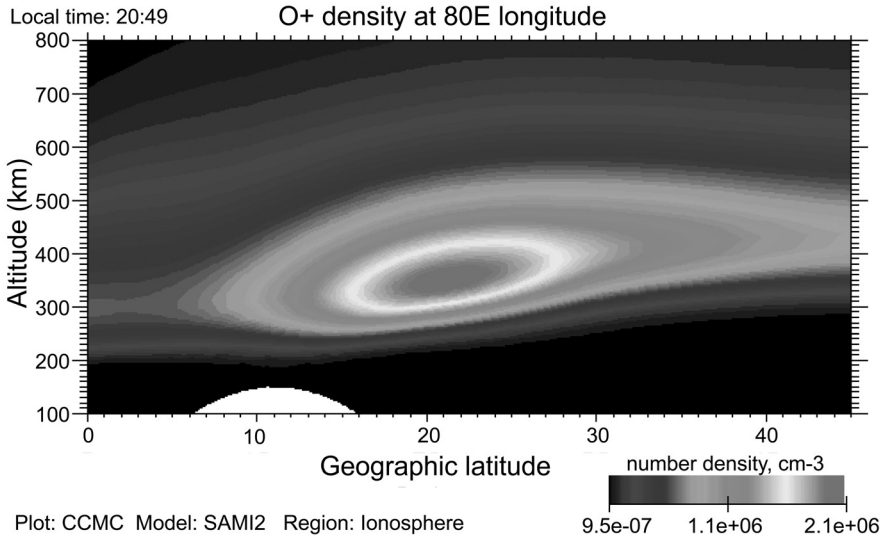

Figure 2. Calculated O^+ densities from the SAMI2 model. Simulated conditions are for 80°E, 2049 local time, for day 121 of 2002, F10.7 = 181 × 10^{-22} Js^{-1} m^{-2} Hz^{-1}, Ap = 5. Image courtesy of the CCMC (ccmc.gsfc.nasa.gov).

whose existence had been hypothesized by *Sagawa et al.* [2005].

[13] Data from the OGO 4 satellite will be used as part of the discussion in sections 3 and 4. The OGO D 12 photometer measured vertical profiles of 630.0 nm emission rates, allowing both the airglow brightness and altitude of the peak brightness to be calculated. Profiles of the emission brightness in the zenithal direction and the altitude of the peak emission along the geographic equator are shown in Figure 4. The high inclination orbit of the OGO 4 satellite allowed complete longitudinal coverage to be sampled in 1 day, in a similar manner to the TIMED data. The data shown here comes from 4 October 1967, and is centered on 2348 LT. During the previous 36 hours, the K_p index had been 3^- or less and October 1967 was close to equinox and close to solar maximum, all of which meet our selection criteria applied to the TIMED and IMAGE data.

3. Longitudinal Structure of the Nighttime *F* Region O^+ Densities

[14] In this section we shall identify the commonalities and account for the differences in the three sets of observations. Using these, we shall describe the characteristics of the observed phenomena which is necessary for the discussion of the underlying processes given in section 4.

[15] Comparing Figures 1 and 3, it can be seen that during the spring equinox of 2002, both FUV and GUVI observed a wave number 4 structure in the longitudinal dependence of the peak airglow brightness and magnetic latitude of this peak. With one instrument alone, it could be argued that this was an artifact of the precession of the satellite orbit and a long-period propagating wave in the *F* region ionosphere, but the different longitudinal sampling of the two instruments makes it clear that at a fixed LT, this is a stationary structure which is present across all longitudes.

[16] Despite the similarities of the FUV and GUVI observations, there are three discrepancies in these results which must be accounted for. The most notable of these is the difference in the magnetic latitude of the peak airglow brightness in each data set. In general, the GUVI data show the peak to occur at around 2–4° magnetic latitude further north than the FUV data. This can be understood in terms of the shape of the O^+ distribution shown in Figure 2 and the different viewing geometries of the two spacecraft. The GUVI analysis uses only data from close-to-nadir observations, whereas the FUV data come from observations at a wide range of spacecraft-to-zenith angles (SZA), typically around 40–60°. GUVI will record the peak brightness at the latitude where the height integrated O^+ density peaks, whereas the FUV data will show the peak brightness to occur where the vector linking the SZA slanted integrated O^+ density peak and the IMAGE spacecraft intersects the 350 km altitude surface. However, provided the shape of the *F* region O^+ distribution does not change significantly with longitude, both of these measures should reveal a similar longitudinal variability in the magnetic latitude of the peak brightness they observe, so a direct comparison between these two quantities is a reasonable for the analysis presented in this paper. The second discrepancy between the FUV and GUVI data may also be explained by this difference in viewing geometry. In general, the FUV data show the peak brightness of the airglow layer to be greater than that in the GUVI data by around 100 Rayleighs. As the FUV analysis assumes that the emissions are coming from a narrow horizontal layer in order to correct for artificial brightening from the slanted viewing angle, and Figure 2 shows the O^+ distribution itself to be slanted rather than horizontal, it may be expected that the FUV data would show a different absolution value of the airglow brightness to the GUVI data. However, as the absolute brightness of the airglow is less important to the analysis presented here than the relative changes in that brightness, attempting a higher-order correction to the brightness observed by FUV this is not necessary. The third discrepancy between these data is that the plot of magnetic latitude of the peak

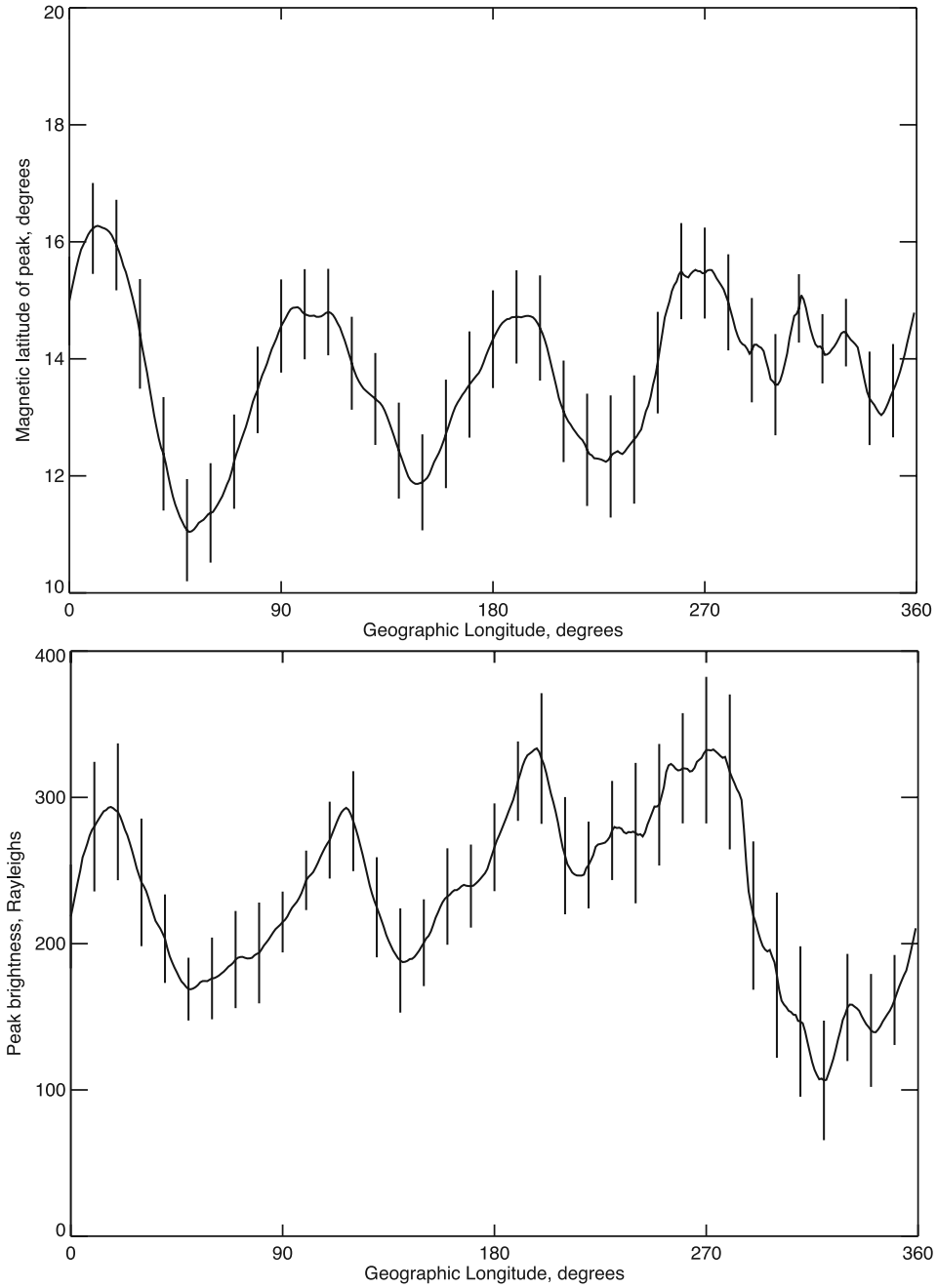

Figure 3. Same as Figure 1, but for IMAGE FUV. Data from 2030 to 2130 LT, between 20 March and 20 April 2002 during magnetically quiet periods are used. Column emission rates have been calculated from line-of-sight emission rates using a simple cosine relationship. A peak emission altitude of 350 km has been assumed for the mapping to geomagnetic coordinates. Gaussian fits to 15 min samples of the data have been used. The solid line represents a ten degree running mean of the peak and location of the peak of these Gaussians. Errors from both spread in the data and uncertainty in the mapping are shown every ten degrees.

emission rates against geographic longitude for the FUV data appears to show some evidence of a fifth peak around 300° longitude, which is not present in the GUVI data. This coincides with the global minimum in airglow brightness observed by both FUV and GUVI, and high SVA for the FUV observations, so the accuracy of the mapping to geographic coordinates and subsequent Gaussian fits to the data in this region may be significantly less than in other regions. Given this, and as the trends at all other longitudes for both the peak brightness and magnetic latitude of that peak show good agreement between the FUV and GUVI data, we shall treat the FUV and GUVI data as both showing the same wave number four longitudinal structure.

[17] Considering the longitudinal variations in both the peak brightness and magnetic latitude of that peak in both

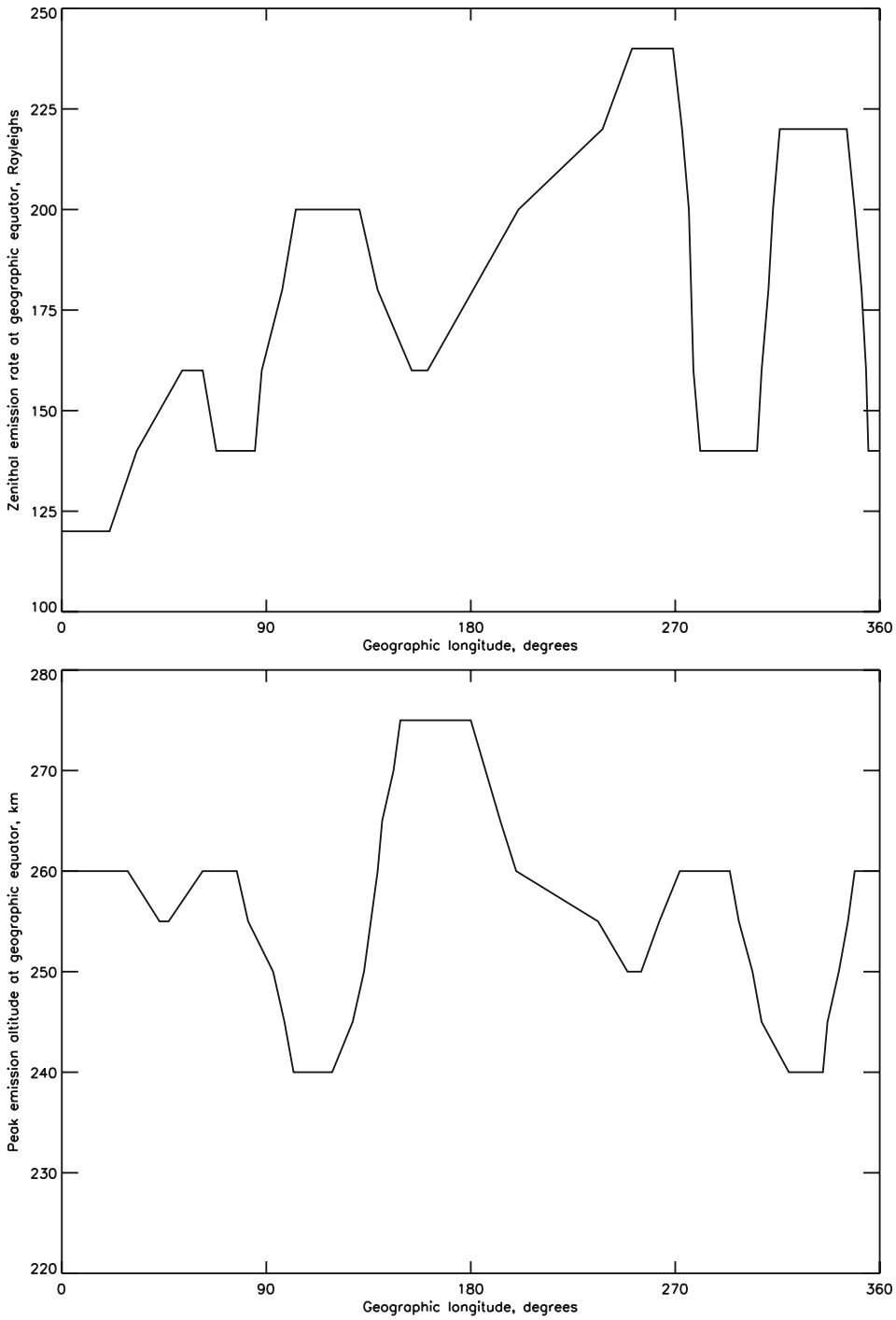

Figure 4. (top) Computed 630.0 nm emission rates in the zenith direction and (bottom) peak emission altitude from OGO D 12 observations during 4 October 1967. Data are for around 2348 LT. Data are from *Thuillier et al.* [1973].

the FUV and GUVI data, it can be seen that both of these quantities vary in phase with one another. Further, as the 135.6 nm nighttime emission depends on the product of the ionospheric O^+ and E densities, this shows that the ion densities are increasing in the locations where the magnetic latitude of the peak emission also increases. GUVI observations of the symmetry between the northern and southern arcs show that the two arcs move further apart in these four locations.

[18] The OGO data in Figure 4 shows the brightness and altitude of the peak 630.0 nm emission along the geographic equator at 2348 LT. Nighttime 630.0 nm emissions come from the deexcitation of $O(^1D)$. This is primarily produced in a charge exchange/recombination reaction involving O^+ and O_2 and hence depends on the concentration of both of these species. As the O_2 concentrations decrease exponentially with height, the 630.0 nm emissions are very sensitive to the emission altitude, and indeed this has been shown to

dominate over moderate changes in O^+ concentrations [*Thuillier and Blamont*, 1973]. This explains why the emission brightness and peak emission altitude shown in Figure 4 are seen to vary out of phase with one another. For this reason, they are also strongly dependent upon meridional neutral wind motions in the *F* region, which move plasma up and down the magnetic field lines, which explains the main north/south asymmetry of the OGO D 12 observations in magnetic coordinates [*Thuillier and Blamont*, 1973; *Thuillier et al.*, 1976].

[19] The OGO D 12 observations can be compared to the FUV and GUVI data only after also accounting for the difference in LT between the observations. As the OGO D 12 data comes from several hours later in the evening, the effects of nighttime neutral winds, which predominantly flow towards the geographic equator around equinox, are more prevalent in this data than the FUV and GUVI data. By 2348 LT, this has altered the two emission arcs such that in the region where the magnetic equator lies to the south of the geographic equator (approximately 180–330° longitude), only the northern arc is visible and in the region where the magnetic equator lies to the north of the geographic equator, only the southern arc is visible [see *Thuillier and Blamont*, 1973, Figure 4]. This means that the peak 630.0 nm emission rates lie approximately along the geographic equator by 2348 LT. For this reason, the emission rates and emission altitudes along the geographic equator are show here, rather than following a magnetic coordinate system which might appear to follow from our treatment of the FUV and GUVI data. In addition, it should also be noted that at this later LT, any structure in the airglow will have drifted further eastward with the background plasma flow with respect to the FUV and GUVI data. A drift of around 10° longitude would be consistent with the drifts measured by the FUV during this time period, compared with ~3–5° by 2100 LT [*Immel et al.*, 2003; *Sagawa et al.*, 2005]. As *Sagawa et al.* [2005] have demonstrated, the basic longitudinal structure of the 135.6 nm emissions is essentially unchanged until at least 0000 LT, once its eastward drift has been accounted for, so the comparison with the OGO D 12 data is valid.

[20] The OGO D 12 data can now be compared to the FUV and GUVI data in order to gain additional insight into the altitude variations of the O^+ layer as a function of longitude. Figure 4 shows that the altitude of the peak 630.0 nm emission varies as a function of longitude, showing a similar wave number four structure as the FUV and GUVI magnetic latitude of the peak emissions (after accounting for the LT effects described above). This shows that the O^+ population is being lifted to higher altitudes at four locations in the equatorial region, where the production rates are highest, and this plasma then diffuses downwards and out to higher magnetic latitudes as it follows the magnetic field lines. This equates to a preferential strengthening of the fountain effect and the associated electric fields at four longitudes. As the 630.0 nm are dependent upon both the O^+ and O_2 concentrations, it is not possible to decouple the altitude and plasma concentration effects on the emission rates observed by OGO 4 and the lack of altitude information in the FUV and GUVI observations mean that it is not possible to quantify the altitude variation of the peak in the O^+ layer and hence the change in strength of the fountain from these observations alone. Only by combining both types of observations can we describe the longitudinal variability in such a complete manner.

[21] From the modulation of the brightness observed by FUV and GUVI, it can be seen that changes in the O^+ concentrations of order 20% would be required to produce the observed effects. As this varies in phase with the change in the strength of the fountain, it follows that continuous plasma production is occurring at the time when the plasma is being lifted to higher altitudes. This is a clear indicator that the controlling process in producing the observed wave number four signature is the dayside fountain, and not the prereversal enhancement, which occurs around the time at which photoionization ceases. The underlying processes responsible for modulating the dayside fountain will be explored in the following section.

[22] Further insight can be gained from other FUV and GUVI observations which have been presented by *Sagawa et al.* [2005] and *Henderson et al.* [2005a]. The wave number 4 signature is observed to persist throughout the evening from 2000 LT up to at least 0000 LT and drifts eastward with the background plasma flow. This shows that whatever processes are involved in the formation of this structure have ceased by 2000 LT, adding further weight to the argument that modulation of the dayside fountain is responsible for the observed structure. During 2002, this wave number 4 signature was present intermittently from day 60 until day 160 (only present on magnetically quiet days) and is seen to return in October of 2002. However, it is not seen during every observed equinox or during any solstice periods, which indicates that at times other processes such as cross-equator winds can dominate over the process responsible for creating this wave number four structure. It is not clear from the results presented here if close-to-solar-max conditions are required to create the wave number 4 structure, but away from solar maximum the 135.6 nm emission rates fall rapidly, making extended observations with FUV impossible and observations with GUVI more difficult and less accurate. Additional data from other sources would be required to investigate this further.

4. Modulation of the Dayside *E* Region Dynamo With Longitude

[23] Using the key points highlighted in the previous section, it is possible to describe the most likely mechanism responsible for creating the observed wave number four structure in the equatorial airglow bands. The dayside *E* region dynamo is driven by eastward electric fields which are primarily set up by eastward Pedersen currents, which are in turn driven by poleward neutral winds in the dayside thermosphere at *E* region altitudes [*Tarpley*, 1970]. Any process which can modulate either these winds or the electric fields they create could modify the dynamo and hence the equatorial fountain.

[24] While topside drivers such as penetration magnetic fields can strongly affect the equatorial fountain, it is difficult to imagine how such drivers might produce a wave number four longitudinal structure which remains fixed over specific longitudes through almost 100 days. Coupling to the lower atmosphere must therefore be considered as the most likely source of this structure. A spectrum of atmospheric tides propagates up from the lower and middle

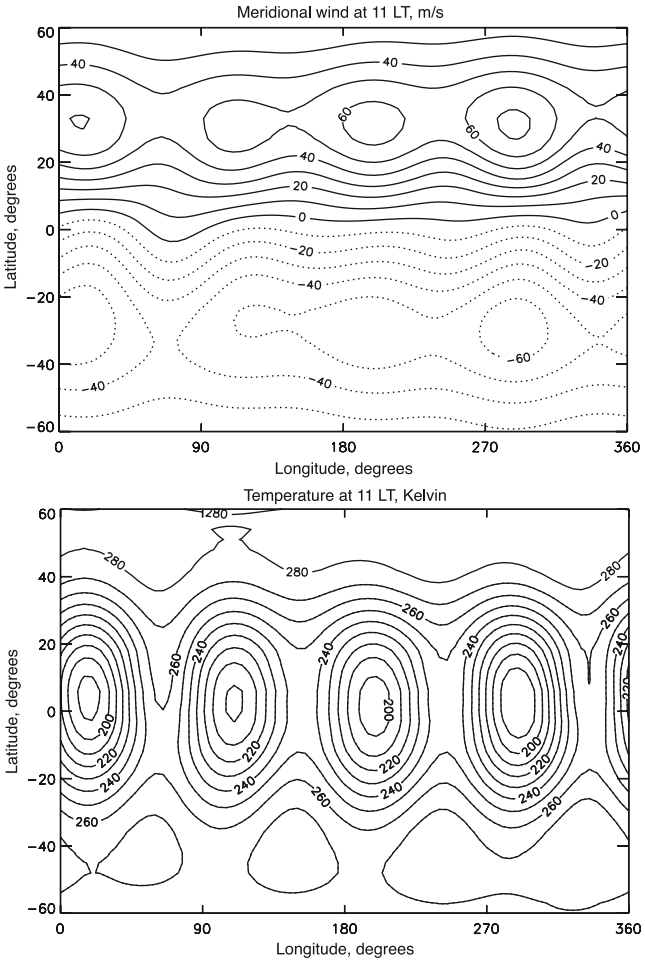

Figure 5. Horizontal structure of the (top) meridional winds and (bottom) temperatures associated with the combined background mean and 13 principal diurnal tidal modes simulated by the GSWM-02 for April at 111 km altitude and 1100 LT. Positive wind values denote northward winds.

atmosphere and strongly modifies the wind and temperature of the lower thermosphere. In the equatorial region, the largest amplitude diurnal modes at *E* region heights are the westward wave number one migrating tide (W1) and the eastward wave number three nonmigrating tide (E3). W1 is strongly excited by radiative heating of the troposphere, with additional contributions from radiative heating in the stratosphere, mesosphere and lower thermosphere [*Forbes*, 1982]. When this wave is viewed in a constant LT reference frame, has no significant longitudinal variation in its amplitude and thus does not produce any modulation of the strength of the equatorial dynamo with longitude. E3 is strongly excited by latent heat release in the troposphere, which is greatest over the tropical rainforest regions [*Hagan and Forbes*, 2002]. When this wave is viewed in the westward rotating LT reference frame, the amplitude of the associated winds and temperatures appear as a four peaked longitudinal structure. It is primarily this wave which modifies the longitudinal structure of the net wind and temperature in the lower thermosphere.

[25] This can be seen in Figure 5, which shows the meridional wind and temperature structure (the background mean plus the 13 principle diurnal tidal modes) at 111 km altitude, which is close to the height of the peak tidal amplitude (above this altitude the diurnal tidal modes which propagate up from the lower atmospheric layers are rapidly attenuated). These meridional winds and temperatures were calculated using the GSWM-02 tidal model for April conditions and thus corresponds closely to the time period of the FUV and GUVI data shown in Figures 1 and 3. Values are shown for 1100 LT, which corresponds to the peak in the vertical drift associated with the equatorial fountain. In the four locations where the nonmigrating E3 tidal amplitude maximizes, the meridional winds in the lower thermosphere also maximize. This enhanced wind will preferentially enhance the Pedersen currents in the *E* region, thus modulating the polarization electric fields and dayside fountain. Around midnight, when the tidal winds are in the opposite direction, the *E* region Pedersen conductivity has fallen significantly, so the influence of these tidal modes is not reversed during the evening. A similar four-peaked longitudinal variation is also seen in the thermospheric temperature structure (shown in Figure 5) as this too is strongly modulated by the E3 nonmigrating tide. The possible effects of this are discussed below.

[26] Figure 6 shows the comparison of the low-latitude poleward winds at *E* region altitude with the FUV, GUVI, and OGO D 12 data. The close correspondence between the winds as a function of longitudes and the O^+ density (measured by the peak 135.6 nm emissions) and the strength of the equatorial fountain (measured by the magnetic latitude of the peak 135.6 nm emissions and height of the peak 630.0 nm emissions) is clearly visible.

[27] While modification of the Pedersen currents through modifying the meridional winds in the *E* region seems the most obvious mechanism by which the propagating tidal modes can modify the dayside fountain, it is not possible to say that this is the only mechanism. As the zonal winds are also modulated by the E3 tide, and these winds are not symmetrical about local noon, it is possible that these winds can drive Hall currents, leading to polarization electric fields and hence modification of the dayside fountain. Further, it is also possible that changes in the temperature and density of the lower thermosphere associated with these propagating tidal modes could alter the *E* region electron densities and hence the polarization electric fields responsible for the dayside fountain, by altering dayside ion production rates (which *Monro et al.* [1976] used to explain the local time asymmetry about noon in the *E* region ionosphere). From the correlation between the lower thermosphere winds or temperatures and strength of the dayside fountain alone, it is not possible to comment on the relative importance of these three possible causal routes, although it seems likely that some combination of all three will be responsible for the observed effects. Using a time-dependent electrodynamics model, which takes into account the phase and vertical structure of the propagating tidal modes as well as the background mean, it should be possible to show how large an impact on the equatorial fountain could be explained by each of these three individually as well as their combined effect, but such a simulation is beyond the scope of this paper. Previous model studies of the impact of propagating

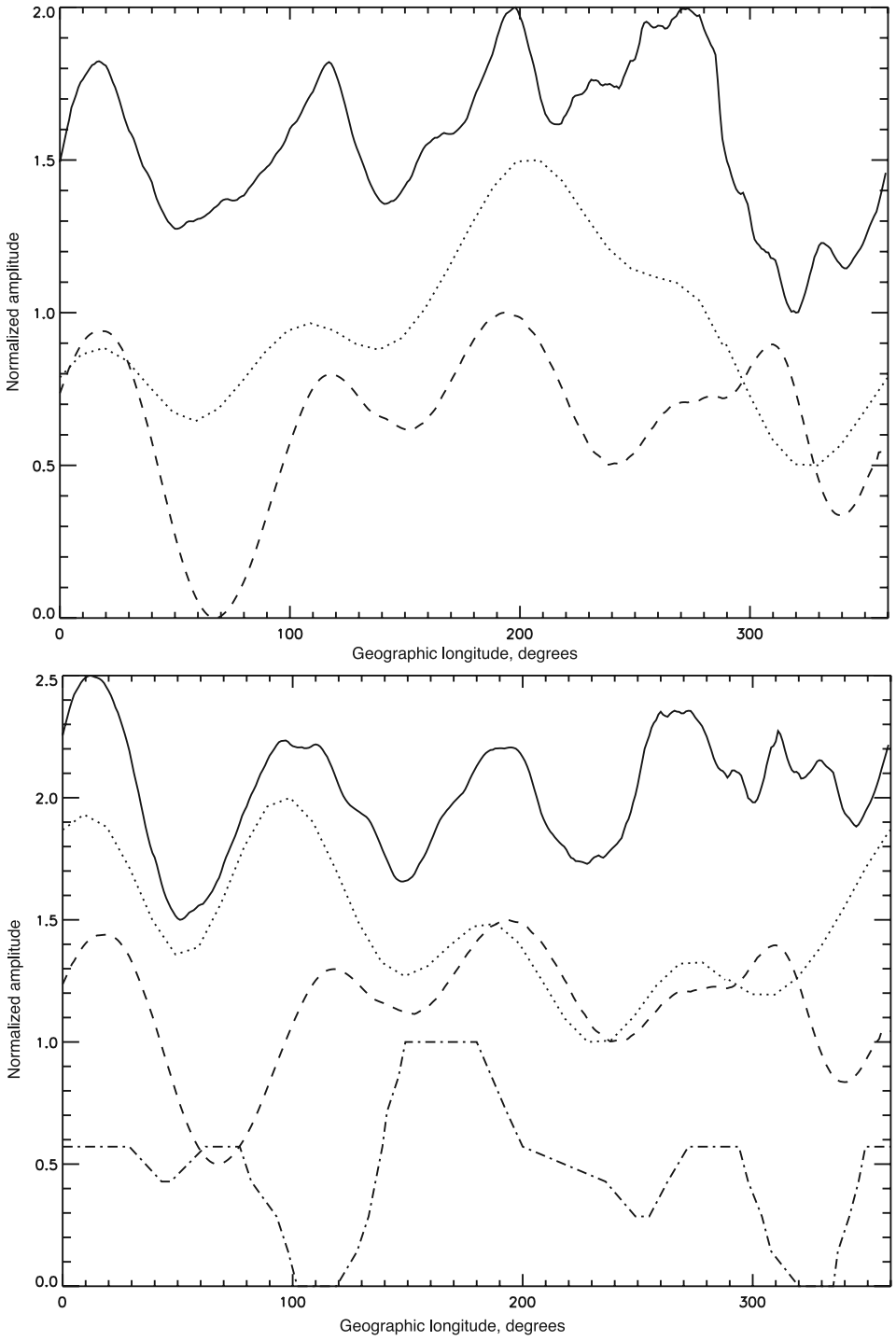

Figure 6. (top) Comparison of the peak brightness observed by FUV and GUVI to the poleward winds from the GSWM-02 model at 111 km altitude and 1100 LT. All amplitudes have been normalized to a scale of 0–1. The solid line represents the FUV data and has been offset by 1.0; the dotted line represents the GUVI data and has been offset by 0.5; the dashed line represents the poleward winds averaged over ±15–20° magnetic latitude. (bottom) As for the top but for the magnetic latitude of the peak brightness observed by FUV and GUVI, the poleward winds at 111 km and 1100 LT from the GSWM-02 model and the height of the peak emissions from OGO D 12, represented by the dot-dash line. Vertical offsets of 1.5, 1.0, 0.5, and 0.0 have been applied to these values, respectively.

tidal modes on the equatorial fountain effect have yielded apparently mixed results. *Millward et al.* [2000] have reported that propagating tidal modes have very little impact on the equatorial *F* region, whereas *Fesen* [1997] have suggested that modulations of up to 20% in hmF2 and NmF2 can be induced. It is however worth stressing here that neither of the models used in these studies was capable of simulating the wave number four structure of winds and temperatures in the lower thermosphere discussed in here.

[28] In addition to modeling work, other observations may allow the proposed mechanism described here to be explored in more detail. Simultaneous observations of the *E* and *F* region winds, along with the equatorial airglow intensity would be ideal and in this regard the UARS WINDII instrument appears at first to offer a useful data set. Wind and airglow intensity from 630.0 nm emissions observed by WINDII have been used by *Thuillier et al.* [2002] to demonstrate the control of cross-equator winds in the *F* region over the asymmetry of the 630.0 nm emission arcs. Their observations did not show the wave number four signature identified in the OGO D 12 data, but they only considered one day of data from close-to-equinox conditions when the *F* region nighttime wind pattern was far from symmetrical about the equator and with $K_p \leq 5$, which is significantly higher than the periods considered here. Further, while WINDII could offer a useful insight into the nighttime *F* region winds, it could not measure the dayside *E* region winds on the same day, and so this data set does not offer a means of fully testing the theory proposed here. Other global scale observations of the equatorial ionosphere, such as measurements of the equatorial electrojet during this period (such as those made by the Champ satellite) may offer another independent confirmation of the longitudinal structure reported here, and these shall be explored in a future work.

[29] The effect of the prereversal enhancement on the longitudinal structure in the equatorial airglow is also worth considering here. As indicated in section 3, there is persuasive evidence that the process which is controlling the wave number four structure occurs in the dayside ionosphere, but the effects of the prereversal enhancement, if any, are not separable from these when considering airglow observations taken in the early-to-middle evening. Assuming that any external drivers remain constant, and neglecting the wave number one effects discussed in section 1 which are unable to explain the results reported here, there should not be longitudinal variability in the strength of the *F* region dynamo due to processes occurring at *F* region altitudes. However, any modulation of the *E* region dynamo during the daytime is known to affect electron densities in the *F* region, and hence may alter the ratio of the integrated Pedersen conductivities in the two regions, and hence alter the strength of the pre-reversal enhancement [e.g., *Heelis*, 2004]. This will either amplify the wave number four structure set up by the dayside fountain, or at minimum have a negligible impact. This could be further explored if global-scale dayside measurements of the equatorial airglow arcs or associated electron densities existed for the time periods considered here. Disk observations of the dayside 135.6 nm emissions such as those made by FUV and GUVI are not suitable for this as they are not able to identify the emissions from O^+ above the background dayglow of OI. GUVI limb scan observations may offer a means of directly imaging the height variations in the O^+ layer on the dayside ionosphere, but the limb observations during the time period considered here are for an LT of around 0000. Further study of other time periods may enable more direct evidence of the relative influence of the dayside fountain and prereversal enhancement to be found.

[30] *Sagawa et al.* [2005] suggested that the semidiurnal tides in the *E* region could be responsible for creating the observed longitudinal variability in the equatorial 135.6 nm emissions. While the amplitude of the semi-diurnal modes is significant at these altitudes, their impact on the longitudinal structure of the lower thermosphere winds and temperatures does not match the observations as well that made by the diurnal modes [*Immel et al.*, 2006]. Theoretical studies have also indicated that the semidiurnal tides play a lesser role in driving the dayside fountain than the diurnal tides [e.g., *Tarpley*, 1970]. It is not clear what influence these modes have on the longitudinal structure in the airglow, but modeling of this system may be able to quantify their importance.

[31] The observations presented here show no consistent wave number one signature in the strength of the equatorial fountain which has been predicted and reported by other authors as described in section 1. It is not clear why this is the case, but it may be that the lack of horizontal resolution of previous measurements has overplayed the strength of these effects, or that the propagating tides dominate over the longitudinal structure for the seasonal and geospace conditions considered here.

5. Conclusions

[32] A process which modifies the dayside equatorial ionospheric fountain has been observed to create a longitudinal wave number four pattern in the *F* region ion density, peak altitude and magnetic latitude of the peak densities. A consistent set of observations from IMAGE FUV, TIMED GUVI, and OGO D 12 have shown that this structure is present in the postsunset ionosphere and lasts until at least midnight. This structure is observed to be present over several months around several equinoxes during magnetically quiet periods close to solar maximum but is dominated by other processes such as cross-equator winds and penetrations electric fields during other periods. A good correlation between the tidally modulated winds and temperatures in the lower thermosphere and the in the equatorial anomaly indicates that they are provide the most likely mechanism responsible for the longitudinal structure within the EIA. This may occur through the longitudinal variation in the thermospheric winds which drive the dynamo effect or through a variation in the optical depth of the thermosphere and hence the ion production rate, or a combination of these effects. It is not clear form this study what role, if any the pre-reversal enhancement and semidiurnal tides at *E* region altitudes have in producing the observed effects in the EIA. Further studies using coupled electrodynamics models and observations such as presunset ion densities may help to quantify these effects. The results presented here highlight the importance of understanding the temporal variability of tropospheric weather systems on our understanding and possible pre-

dictability of the development of the *F* region ionosphere. They may also provide a possible further means of testing our understanding of atmospheric tides on a global scale.

[33] **Acknowledgments.** The IMAGE FUV instrument is supported by NASA at the University of California Berkeley. IMAGE FUV analysis is supported by NASA through Southwest Research Institute subcontract number 8382 at the University of California, Berkeley under contract NAS5-96020. The TIMED GUVI analysis was supported under NASA grant NAG5-5001 through the Aerospace Corporation under grant JO-7415. GSWM results are achieved on the CEDAR Data System at the National Center for Atmospheric Research sponsored by the National Science Foundation.

[34] Zuyin Pu thanks George Millward and Joseph Huba for their assistance in evaluating this paper.

References

Appleton, E. V. (1946), Two anomalies in the ionosphere, *Nature*, *157*, 691.

Bramley, E. N., and M. Young (1968), Winds and electromagnetic drifts in the equatorial F2 region, *J. Atmos. Terr. Phys.*, *30*, 99–111.

Challinor, R. A., and D. Eccles (1971), Longitudinal variations of the mid-latitude ionosphere produced by neutral-air winds-I: Neutral-air winds and ionospheric drifts in the northern and southern hemispheres, *J. Atmos. Terr. Phys.*, *33*, 363–369.

Christensen, A. B., et al. (2003), Initial observations with the Global Ultraviolet Imager (GUVI) in the NASA TIMED satellite mission, *J. Geophys. Res.*, *108*(A12), 1451, doi:10.1029/2003JA009918.

Eccles, D., J. W. King, and P. Rothwell (1971), Longitudinal variations of the mid-latitude ionosphere produced by neutral-air winds-II: Comparisons of the calculated variations of electron concentration with data obtained from the Ariel I and Ariel III satellites, *J. Atmos. Terr. Phys.*, *33*, 371–377.

Farley, D. T., E. Bonelli, B. G. Fejer, and M. F. Larsen (1986), The prereversal enhancement of the zonal electric field in the equatorial ionosphere, *J. Geophys. Res.*, *91*, 13,723–13,728.

Fejer, B. G., E. R. dePaula, S. A. Gonzalez, and R. F. Woodman (1991), Average vertical and zonal F region plasma drifts over Jicamarca, *J. Geophys. Res.*, *96*, 13,901–13,906.

Fesen, C. G. (1997), Theoretical effects of tides and auroral activity on the low-latitude ionosphere, *J. Atmos. Sol. Terr. Phys.*, *59*, 1521–1532.

Forbes, J. M. (1982), Atmospheric tides: 1. Model description and results for the solar diurnal component, *J. Geophys. Res.*, *87*, 5222–5240.

Hagan, M. E., and J. M. Forbes (2002), Migrating and nonmigrating diurnal tides in the middle and upper atmosphere excited by tropospheric latent heat release, *J. Geophys. Res.*, *107*(D24), 4754, doi:10.1029/2001JD001236.

Hanson, W. B., and R. J. Moffett (1966), Ionization transport effects in the equatorial *F* region, *J. Geophys. Res.*, *71*, 5572–5599.

Heelis, R. A. (2004), Electrodynamics in the low and middle latitude ionosphere: a tutorial, *J. Atmos. Sol. Terr. Phys.*, *66*, 825–838.

Henderson, S. B., C. M. Swenson, A. B. Christensen, and L. J. Paxton (2005a), Morphology of the equatorial anomaly and equatorial plasma bubbles using image subspace analysis of Global Ultraviolet Imager data, *J. Geophys. Res.*, *110*, A11306, doi:10.1029/2005JA011080.

Henderson, S. B., C. M. Swenson, J. H. Gunther, A. B. Christensen, and L. J. Paxton (2005b), Method for characterization of the equatorial anomaly using image subspace analysis of Global Ultraviolet Imager data, *J. Geophys. Res.*, *110*, A08308, doi:10.1029/2004JA010830.

Huba, J. D., G. Joyce, and J. A. Fedder (2000), Sami2 is another model of the ionosphere (SAMI2): A new low-latitude ionosphere model, *J. Geophys. Res.*, *105*, 23,035–23,053.

Humm, D. C., et al. (1998), Design and performance of the Global Ultraviolet Imager (GUVI), *Proc. SPIE*, *3445*, 2–12.

Immel, T. J., S. B. Mende, H. U. Frey, L. M. Peticolas, and E. Sagawa (2003), Determination of low latitude plasma drift speeds from FUV images, *Geophys. Res. Lett.*, *30*, 1945, doi:10.1029/2003GL017573.

Immel, T. J., E. Sagawa, S. L. England, S. B. Henderson, M. E. Hagan, S. B. Mende, H. U. Frey, C. M. Swenson, and L. J. Paxton (2006), The control of equatorial ionospheric morphology by atmospheric tides, *Geophys. Res. Lett.*, *33*, L15108, doi:10.1029/2006GL026161.

Kato, S. (1956), Horizontal wind-systems in the ionospheric *E* region deduced from the dynamo theory of the geomagnetic S_q variation. Part II. Rotating Earth, *J. Geomagn. Geoelectr.*, *8*, 24–37.

Kato, S. (1957), Horizontal wind systems in the ionospheric E region deduced from the dynamo theory of the geomagnetic Sq variation. Part IV, *J. Geomagn. Geoelectr.*, *9*, 107–115.

Lyon, A. J., and L. Thomas (1963), The F2-region equatorial anomaly in the African, American and East Asian sectors during sunspot minimum, *J. Atmos. Terr. Phys.*, *25*, 373–386.

Martyn, D. F. (1947), Atmospheric tides in the ionosphere. I. Solar tides in the F2 region, *Proc. R. Soc. London, Ser. A*, *189*, 241–260.

Martyn, D. F. (1953), Electric currents in the ionosphere. III. Ionization drift due to winds and electric fields, *Phil. Trans. R. Soc. London, Ser. A*, *246*, 306–320.

Mende, S. B., et al. (2000a), Far ultraviolet imaging from the IMAGE spacecraft. 1. System design, *Space Sci. Rev.*, *91*, 243–270.

Mende, S. B., et al. (2000b), Far ultraviolet imaging from the IMAGE spacecraft. 2. Wideband FUV imaging, *Space Sci. Rev.*, *91*, 271–285.

Millward, G. H., I. C. F. Müller-Wodarg, A. D. Aylward, T. J. Fuller-Rowell, A. D. Richmond, and R. J. Moffett (2000), An investigation into the influence of tidal forcing on *F* region equatorial vertical ion drift using a global ionosphere thermosphere model with coupled electrodynamics, *J. Geophys. Res.*, *106*, 24,733–24,744.

Monro, P. E., J. S. Nisbet, and T. L. Stick (1976), Effects of tidal oscillations in the neutral atmosphere on electron densities in the *E* region, *J. Atmos. Terr. Phys.*, *38*, 523–528.

Namba, S., and K.-I. Maeda (1939), *Radio Wave Propagation*, Corona, Tokyo.

Paxton, L. J., et al. (1999), Global ultraviolet imager (GUVI): measuring composition and energy inputs for the NASA Thermosphere Ionosphere Mesosphere Energetics and Dynamics (TIMED) mission, *Proc. SPIE*, *376*, 265–276.

Rishbeth, H. (1971), Polarization fields produced by winds in the equatorial *F* region, *Planet. Space Sci.*, *19*, 357–369.

Sagawa, E., T. J. Immel, H. U. Frey, and S. B. Mende (2005), Longitudinal structure of the equatorial anomaly in the nighttime ionosphere observed by IMAGE/FUV, *J. Geophys. Res.*, *110*, A11302, doi:10.1029/2004JA010848.

Tarpley, J. D. (1970), The ionospheric wind dynamo-II solar tides, *Planet. Space Sci.*, *18*, 1091–1103.

Thomas, L. (1968), The F2-region equatorial anomaly during solstice periods at sunspot minimum, *J. Atmos. Terr. Phys.*, *30*, 1631–1640.

Thuillier, G., and J. E. Blamont (1973), Vertical red line 6300 Å distribution and tropical nightglow morphology in quiet magnetic conditions, in *Physics and Chemistry of Upper Atmospheres*, edited by B. M. McCormac, pp. 219–231, Springer, New York.

Thuillier, G., J. W. King, and A. J. Slater (1976), An explanation of the longitudinal variation of O^1D (630 nm) tropical nightglow intensity, *J. Atmos. Terr. Phys.*, *38*, 155–158.

Thuillier, G., R. H. Wiens, G. G. Shepherd, and R. G. Roble (2002), Photochemistry and dynamics in the thermospheric intertropical arcs measured by the WIND Imaging Interferometer on board UARS: A comparison with TIE GCM simulations, *J. Atmos. Sol. Terr. Phys.*, *64*, 405–415.

Vladimer, J. A., P. Jastrzebski, M. C. Lee, P. H. Doherty, D. T. Decker, and D. N. Anderson (1999), Longitudinal structure of ionospheric total electron content at low latitudes measured by the TOPEX/Poseidon satellite, *Radio Sci.*, *34*, 1239–1260.

Walker, G. O. (1981), Longitudinal structure of the *F* region equatorial anomaly: A review, *J. Atmos. Terr. Phys.*, *43*, 763–774.

Walker, G. O., J. H. J. Ma, R. G. Rastogi, M. R. Deshpande, and H. Chandra (1980), Dissimilar forms of the ionospheric equatorial anomaly observed in East Asia and India, *J. Atmos. Terr. Phys.*, *42*, 629–635.

Woodman, R. F. (1970), Vertical drift velocities and east-west electric fields at the magnetic equator, *J. Geophys. Res.*, *75*, 6249–6259.

S. L. England, H. U. Frey, T. J. Immel, and S. B. Mende, Space Sciences Laboratory, University of California, Berkeley, Berkeley, CA 94720, USA. (england@ssl.berkeley.edu)

M. E. Hagan, High Altitude Observatory, National Center for Atmospheric Research, P. O. Box 3000, Boulder, CO 80307, USA.

S. B. Henderson and C. M. Swenson, Department of Electrical and Computer Engineering, Utah State University, Logan, UT 84322, USA.

L. J. Paxton, Johns Hopkins University Applied Physics Laboratory, Laurel, MD 20723, USA.

E. Sagawa, National Institute of Information and Communications Technology, 4-2-1 Nukui-Kitomachi, Koganei, Tokyo 184-9795, Japan.